JOURNAL OF MAGNETIC RESONANCE **131,** 295–309 (1998)
ARTICLE NO. MN971339

Complete Determination of Nitrogen Quadrupole and Hyperfine Tensors in an Oxovanadium Complex by Simultaneous Fitting of Multifrequency ESEEM Powder Spectra

E. J. Reijerse,* A. M. Tyryshkin,†,‡ and S. A. Dikanov†,‡

*Department of Molecular Spectroscopy, University of Nijmegen, Toernooiveld, 6525 ED Nijmegen, The Netherlands; ‡Institute of Chemical Kinetics and Combustion, Novosibirsk 630090, Russia; and †Macromolecular Structure and Dynamics, Pacific Northwest National Laboratory, Richland, Washington 99352

Received April 28, 1997; revised November 17, 1997

One-dimensional C- and X-band as well as two-dimensional X-band ESEEM experiments were performed on the complex oxobis(2-methylquinolin-8-olato) vanadium(IV) in frozen solution. A ^{14}N ESEEM simulation strategy based on initial first- and second-order perturbation analysis of peak positions in orientationally selected ESEEM spectra is presented. The constraint parameters extracted enable one to reduce the number of free fitting parameters for each nitrogen from 10 to 4. These are the α, β resp. the ϕ, θ Euler angles of the NQI and the HFI tensor defined in the coordinate system of the axial g tensor. The local symmetry of the complex allows one to reduce the number of free parameters to two angles only. Subsequently, a grid search in the remaining Euler space produced the starting parameters for the final fit of the ^{14}N hyperfine and quadrupole tensors. The anisotropic nitrogen hyperfine interaction tensor was found to be strongly nonaxial (0.06, 0.51, −0.57) MHz with the components significantly smaller than the isotropic hyperfine constant −6.18 MHz. In contrast, the quadrupole tensor with $K = 0.58$ MHz is close to axial ($\eta = 0.13$). These tensors share the principal axis normal to the ligand plane (as imposed by the local symmetry). The axes in the ligand plane are, however, rotated 50° with respect to each other. The orientation of the quadrupole tensor axes correlate within 10° with the orientation of the ligand plane following from the X-ray structure.

INTRODUCTION

The characterization of nitrogen-coordinated oxovanadium complexes in inorganic (*1–9*) and biological systems (*10–18*) using advanced EPR techniques has been a subject of interest for many years. It has been demonstrated that through the measurement of ESEEM spectra at orientation-selective positions in the anisotropic EPR spectra, the type of coordination and nature of the nitrogen-containing ligands can be determined.

The anisotropy of the hyperfine interaction (hfi) of the directly coordinated equatorial nitrogen in VO^{2+} is usually quite small (few tenths of a megahertz) and ESEEM spectra are governed by a significant isotropic hfi (5–7 MHz) leading to dominating double-quantum features. In addition, at the orientation-selection positions close to the ''single-crystal-like'' conditions, the lines from single-quantum transitions as well as the combination peaks in two-pulse spectra are usually well pronounced. Dikanov *et al.* (*16*) derived the second-order analytical expressions for this set of experimental features unlimited by any restrictions on the relative orientation of nitrogen hyperfine and quadrupole tensors and the applied magnetic field. The application of these expressions to the analysis of the frequency positions of the ESEEM signals provides reliable starting values or constraints for hyperfine and quadrupole parameters which significantly simplify the final fitting of the experimental data. As a result of such analysis, the determination of the hyperfine and quadrupole tensors of the coordinating histidine nitrogen in VO^{2+}-substituted D-xylose isomerase was reported (*16*). These tensors have provided a comprehensive magnetic resonance picture of the electronic and geometrical structure of nitrogen coordination in an oxovanadium complex.

The NMR, ENDOR, and ESEEM data obtained for nitrogen quadrupole tensors in L-histidine monochloride monohydrate and Cu^{2+}-doped L-histidine monochloride monohydrate single crystals show that the principal directions of the quadrupole tensor are mainly connected with the ligand molecule itself and thus can be effectively used to characterize the ligand orientation in the complex (*19–22*). This conclusion needs further experimental verification before being applied to the complexes of other metals. The available single-crystal structure for the complex of oxobis(2-methylquinoline-8-olato) vanadium(IV) (VO^{2+}-$(meox)_2$) (*23*) allows one to perform such analysis of the magnetic resonance data for the case of a nitrogen-coordinated oxovanadium. In Fig. 1 the crystal structure of $VO(meox)_2$ is depicted in different projections, revealing the orientation of the VO-bonding axis in the ligand plane.

1090-7807/98 $25.00

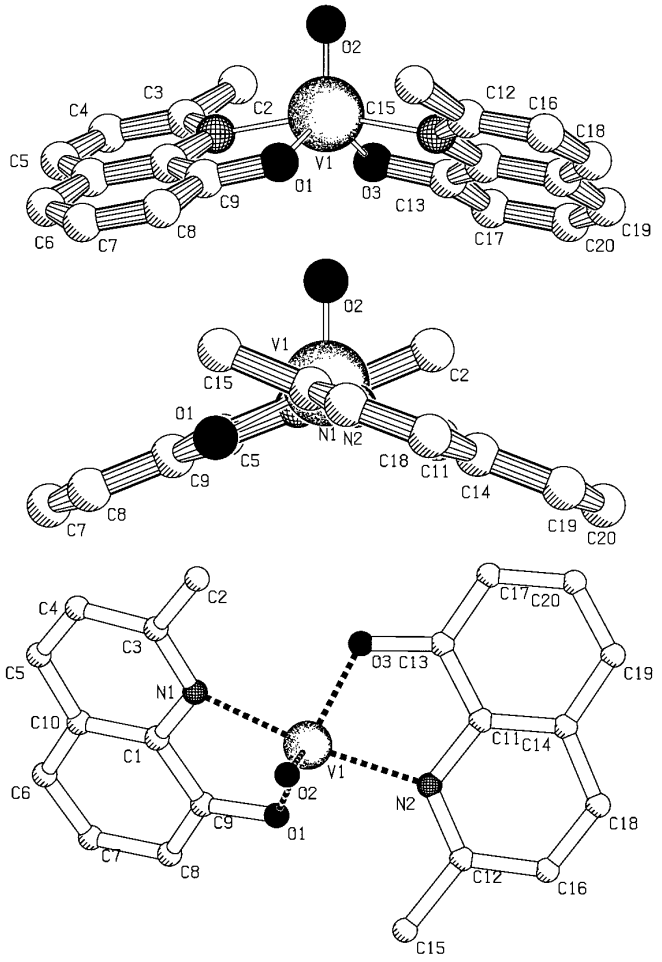

FIG. 1. Structure of the complex $VO(meox)_2$ in three projections indicating the polar angles of the VO unit with respect to the quinoline ligand planes.

The aim of the present work includes the report of 1D C-band and X-band ESEEM experiments as well as 2D X-band HYSCORE experiments on $VO^{2+}(meox)_2$ in frozen solution. The second-order contribution to the ^{14}N ESEEM spectra is studied over a range of Zeeman frequencies from 0.623 to 1.274 MHz which is significantly broader than that reported in the previous study (*16*). The initial analysis of the 1D and 2D ESEEM spectra in the regime of strong hyperfine coupling is based on the second-order estimation of 6 out of the 10 interaction parameters. We demonstrate the use of the second-order expressions in a systematic scanning of the parameter space for the hyperfine and quadrupole tensors of the directly coordinating ^{14}N nuclei in $VO(meox)_2$. It is shown, in particular, that the extension of the X-band experiments to C-band experiments and two-dimensional spectroscopy supplies additional information and accuracy in the determination of the initial parameters. This analysis leads to the determination of the hyperfine and quadrupole tensor of the equatorially coordinated nitrogens and their orientation in the *g*-tensor coordinate system. Finally, the correspondence between the crystal structure and the orientation of principal axes of the nitrogen quadrupole tensor obtained by ESEEM in frozen solution is verified.

EXPERIMENTAL

The complex $VO(meox)_2$ was prepared according to a literature procedure (*23*). The experiments were performed on frozen solutions of $VO(meox)_2$ in a 50/50 mixture of CH_2Cl_2 and toluene. The C-band (7.140 GHz) two-pulse ESEEM spectra were recorded on a homebuilt electron spin echo spectrometer (*24*). The X-band ESEEM and HYSCORE spectra were measured on a Bruker ESP380 FT-EPR spectrometer. All experiments were performed at 20 K. For the HYSCORE experiments the following four-step phase cycling scheme was used to cancel unwanted echo crossings: $\pi/2[+x]-\pi/2[+x]-\pi[\mathrm{ph1}]-\pi/2[\mathrm{ph2}]-\mathrm{echo}[\mathrm{asg1}]$ with $\mathrm{ph1} = [+y + y - y - y]$, $\mathrm{ph2} = [+x - x + x - x]$, and $\mathrm{asg1} = [+a - a + a - a]$. Specific information on pulse lengths is provided in the figure legends.

The two-pulse ESEEM time-domain traces were treated with a rigorous background correction procedure: First the logarithm was taken from the normalized time domain (zero baseline). This results in a virtually linear decay. This was fitted with a first-order polynomial or a cubic spline. The log(background) was subtracted. Finally, the time domain was reconstructed by taking the exponential of the remainder and subtracting a value of 1. This procedure effectively divides the modulation pattern by the (exponential) background decay, thus giving a substantial resolution enhancement. More important, it allows one to compare the ''absolute'' modulation intensities (i.e., normalized to the unmodulated part of the echo) with the corresponding spectral simulations. Prior to zero filling, Fourier transform (FT), and phase correction, the time domain signal (both experimental and simulated) was treated with a Hamming window.

Spectral simulations (two-pulse ESEEM and HYSCORE) were performed using dedicated home-written software based upon the Mims expressions for two-pulse ESEEM (*25, 26*) and the HYSCORE expressions derived by Shane *et al.* (*27*). In the two-pulse ESEEM simulations two nuclei were included with interaction tensors respecting the twofold symmetry axis of the complex (i.e., the V═O bonding axis).

RESULTS

The echo-induced EPR spectrum at 20 K (Fig. 2) is typical of axially coordinated VO complexes. The dominating HFI of ^{51}V ($I = 7/2$) provides the main contribution to the anisotropic lineshapes in the spectrum. This spectrum has been analyzed using a second-order fitting program (*28*) producing the following interaction parameters: A_{xx}, A_{yy} =

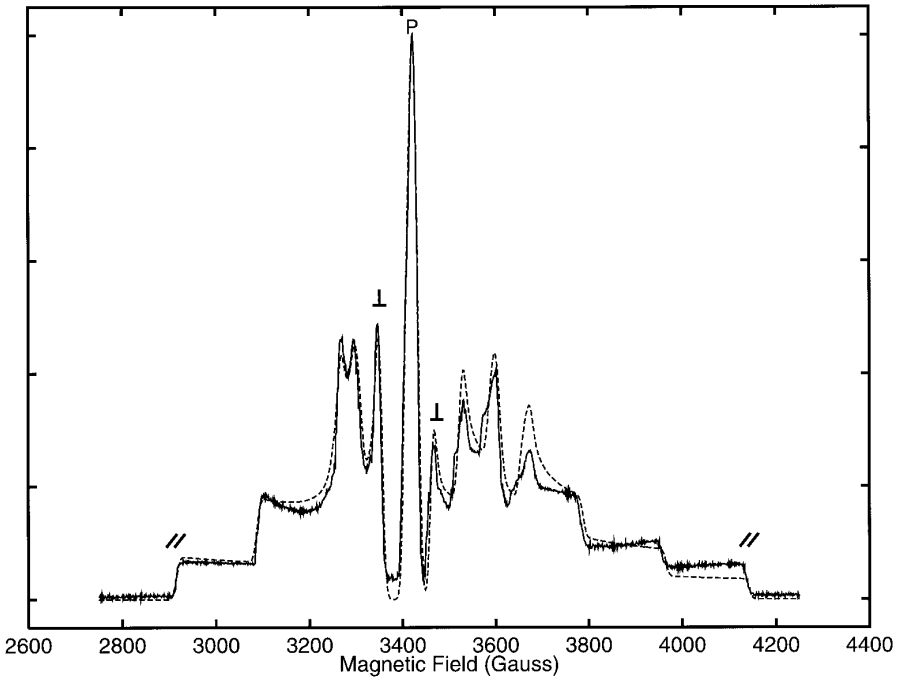

FIG. 2. Echo-induced EPR spectrum of $VO(meox)_2$ at X band. Microwave frequency = 9.7492 GHz; two-pulse sequence: 16/24 ns, τ = 124 ns. The dotted line represents spectral simulation with parameters $g_\perp = 1.97$, $g_\parallel = 1.944$, $A_{xx} = 60.38$, $A_{yy} = 54.40$, and $A_{zz} = 174.42$ G.

55.5, 50.0×10^{-4} cm^{-1}, $A_{zz} = 158.2 \times 10^{-4}$ cm^{-1}, $g_{xx} = g_{yy} = 1.97$, $g_{zz} = 1.944$. These values are virtually identical to the results of Collison *et al.* (*29*) determined in a single crystal.

The positions at which ESEEM spectra were recorded are indicated as ∥ for the parallel orientation-selection region, ⊥ for the perpendicular orientation-selection positions, and ''P'' for the nonorientation-selective (powder) feature. The two-pulse ESEEM spectra corresponding to the three indicated positions at the lower fields are displayed in Fig. 3a (C band) and Fig. 3b (X band). Due to the relatively long transverse relaxation times and the rigorous background correction procedure, the two-pulse FT spectra are exceptionally well resolved, especially at the ∥ position. For instance, the C-band spectrum recorded at a field of 2028 G (nitrogen Zeeman frequency 0.623 MHz) contains five well-pronounced components with positive amplitude at the frequencies 2.10, 3.50, 4.60, 5.64, and 8.04 MHz (±0.02 MHz) which are interpreted as a superposition of two triplets 8.04, 4.60, 3.44 MHz and 5.64, 3.54, 2.10 MHz of six nitrogen nuclear spin transitions from two electron spin manifolds (Table 1a). On changing the magnetic field to 3238 G (ν_I = 0.996 MHz) these two triplets are expected to appear at 8.79, 4.98, 3.82 MHz and 4.89, 3.16, 1.72 MHz, respectively; these values correspond well to the five experimentally observed lines 8.72, 4.88, 3.78, 3.13, and 1.71 MHz in the C-band spectrum at the high-field ∥ position (spectrum not shown). Additionally, the ∥ spectrum at 2028 G contains four narrow lines of negative amplitude which are interpreted as the sum and difference combinations of the double-quantum (13.6, 2.34 MHz) and single-quantum (6.77, 1.20 MHz) transitions. These features are indicated in the spectra as dd+, dd−, ss+, and ss−, respectively. All these peaks except the ss− feature are also observed in the high-field ∥ spectrum at C band (not shown). Similar sets of basic and combination lines are observed in the ∥ spectra recorded at X band. The values of the frequencies and their assignment are listed in Table 1a.

The two-pulse ESEEM spectra measured at the ⊥ and P positions show distinct broadening of the spectral components as compared to the corresponding features at the ∥ positions. Nevertheless, these spectra are also dominated by the double-quantum transitions and the ss+ combination line, which, at these nonselective positions, becomes even more intense. These components have a rather symmetric form in X band and are somewhat distorted in the C-band spectra. This may be due to the smaller splittings between the spectral components at C band leading to stronger dead time artifacts in the cosine FT. The specific property of all C-band spectra is the intense narrow dd− feature. At X band this line is located very close to the dq− peak and its intensity may be masked by the partial overlap. The assigned ⊥ spectral features and their positions are listed in Table 1b.

Additional information on the anisotropy of the nitrogen hyperfine and quadrupole interactions can be obtained from HYSCORE experiments (*24, 27, 30*). This 2D four-pulse

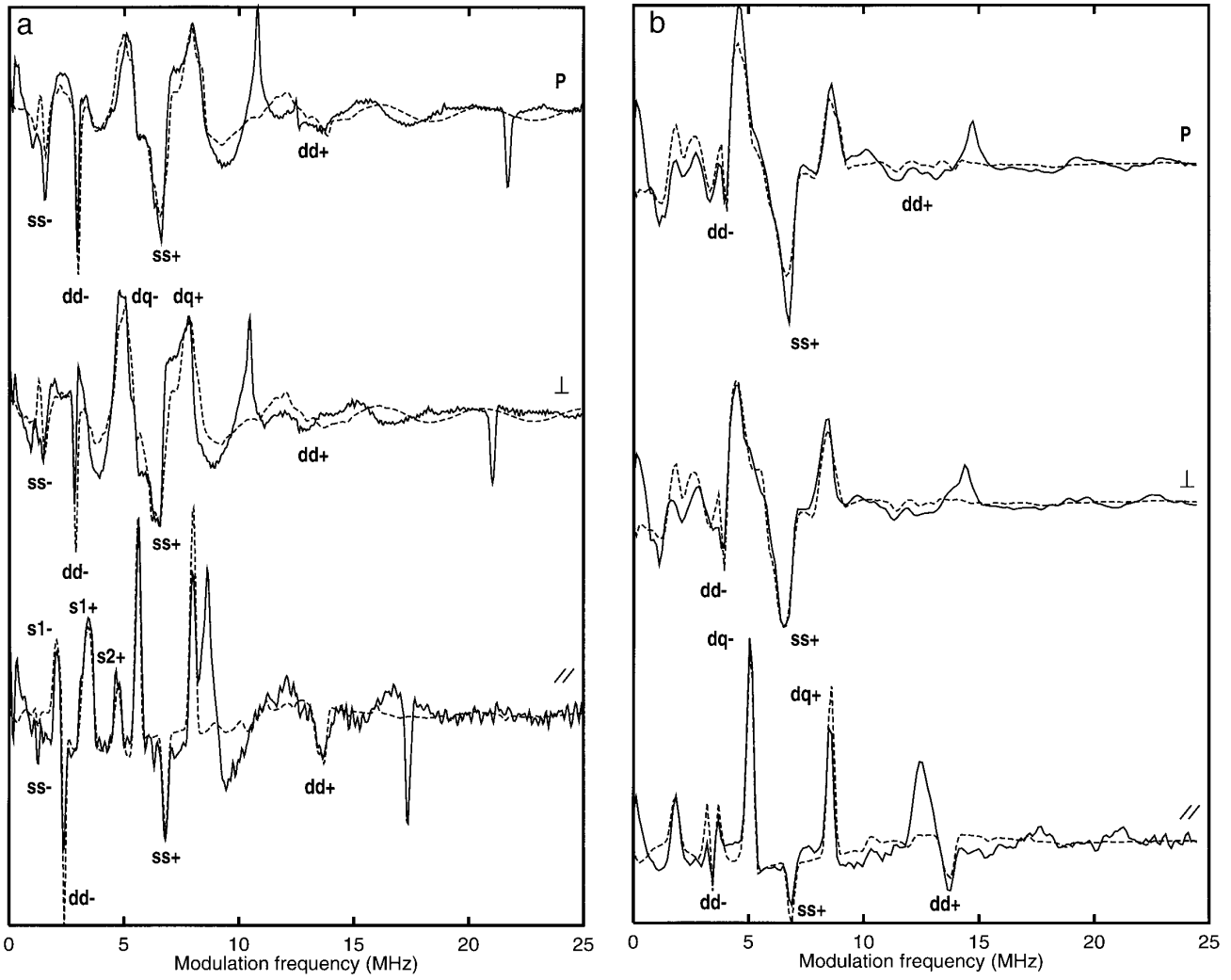

FIG. 3. Primary cosine FT ESEEM experiments on $VO(meox)_2$ at C band (a) and X band (b). Experimental conditions: C band: microwave frequency = 7.140 GHz; pulse sequence, 30 ns$-\tau-$60 ns$-$echo. Step interval = 20 ns, 256 points acquired in 32 scans, 10 echoes per point. Field settings: ∥, 2028 G; ⊥, 2459 G; P, 2534 G. X band: microwave frequency = 9.580 GHz, pulse sequence, 24 ns$-\tau-$32 ns$-$echo. Step interval = 8 ns. Field settings: ∥, 2927 G; ⊥, 3365 G; P, 3429 G. 256 points acquired in 20 scans, 10 echoes per point. The dashed curves represent the simulations using the best-fit parameters as indicated in Table 2.

ESEEM experiment creates cross-correlations ($\pm\nu_{i\alpha(\beta)}$, $\pm\nu_{j\beta(\alpha)}$) between the nuclear frequencies from opposite electron spin manifolds. The HYSCORE experiment is sensitive to the relative signs of correlated frequencies. Therefore, the 2D spectra are typically represented by two quadrants (++) and (+−). The intensities of the peaks with the same frequency coordinates in the (++) and (+−) quadrants are usually different depending on the relative magnitudes of the Zeeman interaction, the hyperfine interaction, and the quadrupole interaction. As the hyperfine coupling increases, the strongest HYSCORE peaks shift from the (++) to the (+−) quadrant.

In Fig. 4 the HYSCORE spectra at the ⊥ position are presented for three different τ values. Clearly, the correlation ridges have the nicest shape at the shortest τ of 124 ns, while for the other values the ridges are distorted by blind spots (*31*). These spectra are typical for nitrogen-coordinated oxovanadium complexes (*9, 24, 27*) and they allow the assignment of each correlation feature.

The 2D correlation features can be labeled analogously to the combination lines in the two-pulse ESEEM experiments, i.e., ''ss+/ss−'' for the sum/difference frequencies of the single-quantum transition, and ''dd−'' for the difference double-quantum combination. As was discussed by Reijerse and Dikanov (*32*) and Höfer (*31*), the projections of the correlation features on the main (positive) diagonal mark the frequency positions of the two-pulse combination lines. The projections on the frequency ordinate axis (as

TABLE 1a
Peak Analysis of ∥ ESEEM Spectra

	C band		X band	
B field [G]:	2028	3238	2927	4144
ν_I [MHz]:	0.623	0.9958	0.900	1.274
$s_+(1)$	3.44	3.78	3.61	3.87
$s_+(2)$	4.60	4.88		5.32
dq_+	8.04	8.72	8.53	9.13
$s_-(1)$	2.10	1.71	1.81	1.64
$s_-(2)$	3.54	3.13	3.24	2.88
dq_-	5.64	4.88	5.07	4.40
ss_+	6.77	6.82	6.83	6.85
ss_-	1.20			
dd_+	13.6	13.6	13.6	13.6
dd_-	2.34	3.78	3.42	4.83
$A_\parallel$	6.41	6.47	6.47	6.48
$A^{(2)}$	1.20	0.97	0.97	0.93
$3Q_\parallel$	1.44	1.42	1.4	1.2
$Q_q = K^2(3 + \eta^2)$ [MHz^2]	1.37	1.14	1.13	1.05

shown in Fig. 4) give the lineshapes of the basic frequencies, largely undistorted by the dead time.

From nine pairs of possible correlation features, only two elongated ridges [$sq_+(1)$, $sq_-(1)$] and [$sq_+(2)$, $sq_-(2)$] between [4.0–6.0, 0.5–2.0] MHz, labeled ''ss+'', have appreciable intensity in the (++) quadrant. We use the notation [$sq_+(1)$, $sq_-(1)$] to denote the *pair* of cross peaks with coordinates [$sq_+(1)$, $sq_-(1)$] and [$sq_-(1)$, $sq_+(1)$]. Another three correlation features are visible in the (+−) quadrant. Here, the highest intensity occurs for the correlation between the double-quantum transitions [$\pm dq_+$, $\mp dq_-$], labeled as ''dd−''. The other set of correlations is due to the single-quantum transitions: [$sq_+(1)$, $sq_-(2)$] and [$sq_+(2)$, $sq_-(1)$]. These features are labeled as ''ss−''. There are also weak indications of correlations between the double-quantum and single-quantum transitions of both manifolds. These, however, do not lead to interpretable features in 1D or 2D ESEEM.

ANALYSIS

Spin Hamiltonian. The spin Hamiltonian describing the electron-nitrogen magnetic interactions in an external magnetic field is expressed as

$$H = \beta \mathbf{B}\cdot\mathbf{g}\cdot\mathbf{S} + \sum_{i=1}^{2}[\mathbf{S}\cdot\mathbf{A}_i\cdot\mathbf{I}_i + \mathbf{I}_i\cdot\mathbf{Q}_i\cdot\mathbf{I}_i - \gamma\hbar\mathbf{B}\cdot\mathbf{I}_i], \quad [1]$$

where $\mathbf{A}_i$ and $\mathbf{Q}_i$ are the HFI and NQI of the coordinating quinoline nitrogens in the complex. In the spectral simulations, the vanadium HFI anisotropy is contained in a ''pseudo'' g tensor since it is relevant only for modeling the effect of orientation selection. The problem is thus reduced to an $S = \frac{1}{2}$, $I = 1$ case.

In the strong field approximation, the electron spin is quantized along the vector $\mathbf{n} = \mathbf{k}\cdot\mathbf{g}/g_{\text{eff}}$, where $\mathbf{k}$ is the direction of the external magnetic field ($\mathbf{B}$). The individual ^{14}N interactions for the two electron spin projections can now be collected into a sub-Hamiltonian:

$$H_\pm = \pm\tfrac{1}{2}\mathbf{n}\cdot\mathbf{A}\cdot\mathbf{I} + \mathbf{I}\cdot\mathbf{Q}\cdot\mathbf{I} - \gamma\hbar\mathbf{B}\cdot\mathbf{I}. \quad [2]$$

The eigenvectors and eigenvalues of Eq. [2] are used to simulate the 1D and 2D ESEEM spectra (*25–27*). Actually, the ^{14}N hyperfine and quadrupole interactions in an axial EPR system like that of VO^{2+} are completely described by 10 parameters, i.e., the principle values of both tensors and their orientation relative to the principal axis of the axial g tensor. These include 6 parameters for the hyperfine tensor (a, the isotropic hyperfine constant; T_1 and T_2, the first two anisotropic principal components; ϕ, θ, and ψ, the Euler angles) and 4 parameters for the quadrupole tensor ($K = e^2qQ/4h$ is the quadrupole coupling constant; η is the asymmetry coefficient; α and β are two Euler angles). The third angle γ characterizing the orientation of the quadrupole tensor is irrelevant in an axial EPR system, and will be set to zero.

Second-order nitrogen frequencies. To first order the energy levels described by the Hamiltonian (*2*) are given by

$$E_n = \pm\tfrac{1}{2}A_n m_I + Q_n(\tfrac{3}{2}m_I^2 - 1) - \nu_I m_I, \quad [3]$$

where A_n and Q_n are the effective HFI and NQI splitting along the direction of the magnetic field. It is assumed that $\mathbf{k}$ and $\mathbf{n}$ coincide. Using the notation of Eq. [3], the second-

TABLE 1b
Peak Analysis of ⊥ ESEEM Spectra

	C-band		X-band
B field [G]:	2459	2579	3481
ν_I [MHz]:	0.7562	0.793	1.071
dq_+(av)	7.92	7.92	8.52
dq_-(av)	4.74	4.98	4.49
ss_-	1.46	1.58	
ss_+(min)	5.5	5.5	
ss_+(max)	6.6	6.5	
dd_-	2.81	2.95	4.04
dd_+(calc)	12.66	12.9	13.01
$A_\perp$(av)	5.91	6.02	6.15
$A^{(2)}$(av)	1.16	1.18	0.95

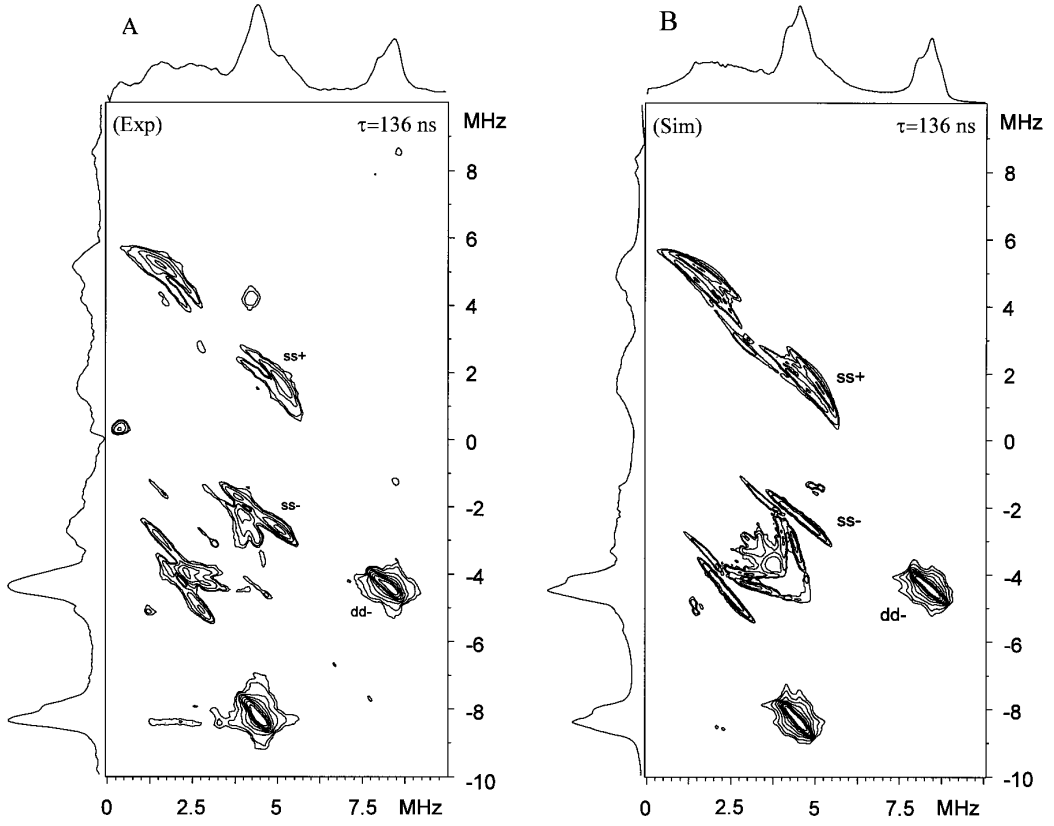

FIG. 4. Experimental (Exp) and simulated (Sim) HYSCORE spectra of $VO(meox)_2$ at X band. The magnetic field was positioned at the $\perp$ position. Experimental conditions: microwave frequency = 9.7492 GHz; pulse sequence, 80 ns $(\pi/2)-\tau-80$ ns $(\pi/2)-T_1-48$ ns $(\pi)-T_2-80$ ns $(\pi/2)-\tau-$echo; 128×128 points in 32-ns steps. Spectral simulations using the best-fit parameters as indicated in Table 2. The correlation features are indicated using the same labels as in Fig. 3. Spectra are labeled as follows: (A) Experiment with $\tau = 136$ ns; (B) simulation corresponding to (A); (C) experiment with $\tau = 200$ ns; (D) simulation corresponding to (C); (E) experiment with $\tau = 480$ ns; and (F) simulation corresponding to (E).

order frequencies of the nitrogen nuclear spin transitions are expressed as

$$\nu_{sq+}^{(1,2)} = \frac{A_n}{2} - \nu_I \pm \frac{3}{2} Q_n + \frac{A^{(2)} \pm Q^{(2)}}{A_n - 2\nu_I}$$

$$\nu_{sq-}^{(1,2)} = \frac{A_n}{2} + \nu_I \pm \frac{3}{2} Q_n + \frac{A^{(2)} \pm Q^{(2)}}{A_n + 2\nu_I}$$

$$\nu_{dq}(\alpha,\beta) = A_n \mp 2\nu_I + \frac{A^{(2)}}{A_n/2 \mp \nu_I}, \qquad [4]$$

where

$$A^{(2)} = \frac{1}{4}(T_{np}^2 + T_{nq}^2) + K^2(3 + \eta^2) - \frac{3}{4} Q_n^2$$

$$Q^{(2)} = 3(Q_{np}T_{np} + Q_{nq}T_{nq}). \qquad [5]$$

The matrix **T** represents the anisotropic part of the HFI. **n** represents the orientation of the external magnetic field; and **p** and **q** are two orientations perpendicular to **n** and to each other. The second-order frequencies of the combination features can now conveniently be derived:

$$\nu_{ss+} = \nu_{sq+}^{(1,2)} + \nu_{sq-}^{(2,1)} = A_n + \frac{A_n A^{(2)} \mp 2\nu_I Q^{(2)}}{2(A_n^2/4 - \nu_I^2)}$$

$$\nu_{ss-} = \nu_{sq+}^{(1,2)} - \nu_{sq-}^{(1,2)} = 2\nu_I - \frac{A^{(2)} \pm Q^{(2)}}{(A_n^2/4 - \nu_I^2)}$$

$$\nu_{dd+} = \nu_{dq+} + \nu_{dq-} = 2A_n + \frac{A_n A^{(2)}}{(A_n^2/4 - \nu_I^2)}$$

$$\nu_{dd-} = \nu_{dq+} - \nu_{dq-} = 4\nu_I - \frac{2\nu_I A^{(2)}}{(A_n^2/4 - \nu_I^2)}. \qquad [6]$$

It will be clear that, in case the second-order theory is applicable, the ss− and dd− frequencies have very little anisotropy (only to second order). This explains the appearance of the narrow peaks near $2\nu_I$ and $4\nu_I$ in all two-pulse ESEEM spectra (Fig. 3). The ss+ and dd+ lines as well as the dq lines are broadened already to first order by the HFI anisotropy. Still they are readily observed in most spectra. The

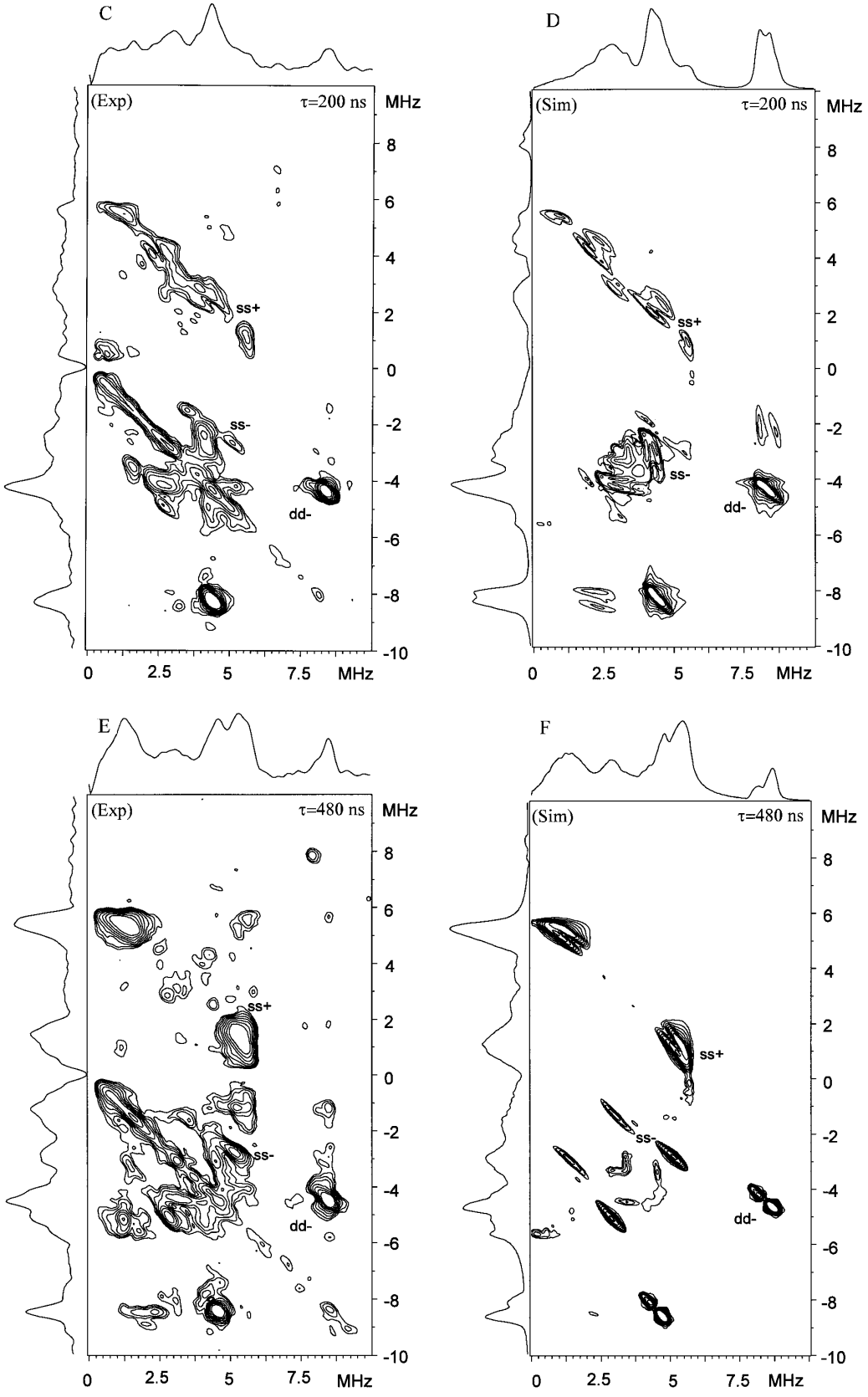

FIG. 4—*Continued*

sq lines ($\nu_{sq\pm}^{(1,2)}$), however, are affected by both HFI and NQR anisotropy, leading to complete broadening except in the ∥ orientation-selective spectra. In the latter ones all lines are beautifully resolved!

Analysis of the ∥ ESEEM spectra. The above expressions are directly applicable to the quantitative analysis of the ESEEM spectra recorded at the ∥ positions. The hyperfine coupling $A_\parallel$ and second-order term $A^{(2)}$ can be calculated from the frequencies of the double-quantum transitions:

$$A_\parallel = \frac{2\nu_I\nu_{dd+}}{8\nu_I - \nu_{dd-}}$$

$$A^{(2)} = \frac{(4\nu_I - \nu_{dd-})(A_\parallel^2/4 - \nu_I^2)}{2\nu_I}. \qquad [7]$$

The $\nu_{dq\pm}$ frequencies can be easily determined from the 1D ESEEM spectra or from the cross peaks in the HYSCORE spectra. The effective quadrupolar splitting $Q_\parallel$ can, in principle, be estimated from the second-order corrected frequencies of the single-quantum transitions:

$$\Delta^+ = \nu_{sq+}^{(1)} - \nu_{sq+}^{(2)} = 3Q_\parallel + \frac{Q^{(2)}}{A_\parallel/2 + \nu_I}$$

$$\Delta^- = \nu_{sq-}^{(1)} - \nu_{sq-}^{(2)} = 3Q_\parallel + \frac{Q^{(2)}}{A_\parallel/2 - \nu_I}. \qquad [8]$$

As it turns out in most cases, the positions of the single-quantum (∥) transitions cannot be determined to sufficient accuracy to allow determination of the $Q^{(2)}$ parameter. Therefore, the $Q_\parallel$ values are estimated using first-order analysis (i.e., neglecting the term $Q^{(2)}/(A_\parallel \pm 2\nu_I)$. $Q_\parallel$ can now be combined with the $A^{(2)}$ parameter (Eq. [5]) to calculate a starting value for the quadrupolar parameter $Q_q = K^2(3 + \eta^2)$. The nonsecular contribution of the HFI ($(T_{np}^2 + T_{nq}^2)/4$) can be neglected in our case (*7, 16*).

In Table 1a, along with the experimental frequencies observed in the ∥ ESEEM spectra of VO(meox)$_2$, the ''constraint parameters'' ($A_\parallel$, $A^{(2)}$, $Q_\parallel$, Q_q) derived for this orientation (using Eqs. [5], [7], and [8]) are summarized.

The first-order hyperfine splitting ($A_\parallel$) along the g_z axis can be expressed in terms of the tensor principal values and the Euler angles:

$$A_\parallel = a + T_\parallel = a + \tfrac{1}{2}\sin^2\theta\{3(T_1 + T_2) + \cos 2\phi(T_1 - T_2)\} - (T_1 + T_2). \qquad [9]$$

The expression for $Q_\parallel$ is analogous and, using the familiar notation in terms of $K = e^2qQ/(4h) = -1/2(Q_3)$ and $\eta = (Q_1 - Q_2)/Q_3$ for the NQI principal values, it will reduce to

$$Q_\parallel = K\{(3 - \eta\cos 2\alpha)\sin^2\beta - 2\}. \qquad [10]$$

Note that in these expressions the convention of Messiah (*33*) was used for the Euler angles, i.e., $R(\alpha, \beta, \gamma) = R_z(\gamma)\cdot R_y(\beta)\cdot R_z(\alpha)$ in passive rotations (i.e., rotation of the coordinate system) and $\mathbf{D}_{lab} = \mathbf{R}\cdot\mathbf{D}_{Principal}\cdot\mathbf{R}^{-1}$. Therefore, the expressions deviate slightly from those published by Dikanov *et al.* (*16*).

Analysis of the ⊥ ESEEM spectra. Although the single-quantum transitions in the ⊥ spectra are broadened beyond detection, the double-quantum and combination lines are still well resolved. Some relevant frequency values extracted from these spectra are summarized in Table 1b. The values for $A_\perp$(av) and $A^{(2)}$ were calculated using Eq. [7]. The basic dq± and combination ss+ features allow one to estimate the anisotropy of the HFI matrix in the ⊥ plane. The extreme values of $A_\perp$ are expressed as

$$A_\perp(1, 2) = a - \tfrac{1}{2}T_\parallel \pm R$$

$$R = \tfrac{1}{4}\{[-3(T_1 + T_2)\sin^2\theta + (T_1 - T_2) \times \cos 2\phi(1 + \cos^2\theta)]^2 + 4(T_1 - T_2)^2\sin^2 2\phi\cos^2\theta\}^{1/2}. \qquad [11]$$

Both the dq± and the ss+ lineshapes are driven mainly by HFI anisotropy (Eqs. [5] and [6]), and parameter R can be directly obtained from the ⊥ spectra as it is related to the extreme positions (bandwidth) of the dq±/ss+ lineshapes (Fig. 3). The values in Table 1b suggest a bandwidth ($2R$) for the C-band ss+ feature of about 1 MHz. The lineshapes of the X-band ss+ features seem to be more narrow (0.7 MHz). Also the dq+ and dq− features both in C and in X band suggest a smaller value. The 2D HYSCORE spectra give an independent way of estimating the anisotropy parameter R. The projection of the ss+ correlation feature on the main diagonal as well as the width of the dd− correlation ridges leads to a bandwidth ($2R$) of around 0.8 MHz. Therefore, R = 0.4 MHz was used as a starting value in the final fitting procedure.

The isotropic contribution, a, to the hyperfine interaction can be estimated from the $A_\parallel$ value (Table 1a) and the average $A_\perp$ value listed as $A_\perp$(av) in Table 1b. Taking the mean values $A_\parallel$ = 6.45 MHz and $A_\perp$(av) = 6.03 MHz, we arrive at a starting value a = 6.17 MHz. In principle, the value for $A^{(2)}$(av) in Table 1b can be used to calculate Q_q using Eq. [5]. If we assume an average value for $Q_\perp$ of $Q_\parallel/2$ = 0.23 MHz, we arrive at Q_q = 1.14, which is very much in the range of the values in Table 1a.

A set of equations analogous to Eq. [11] is available for the effective quadrupole splitting in the ⊥ plane:

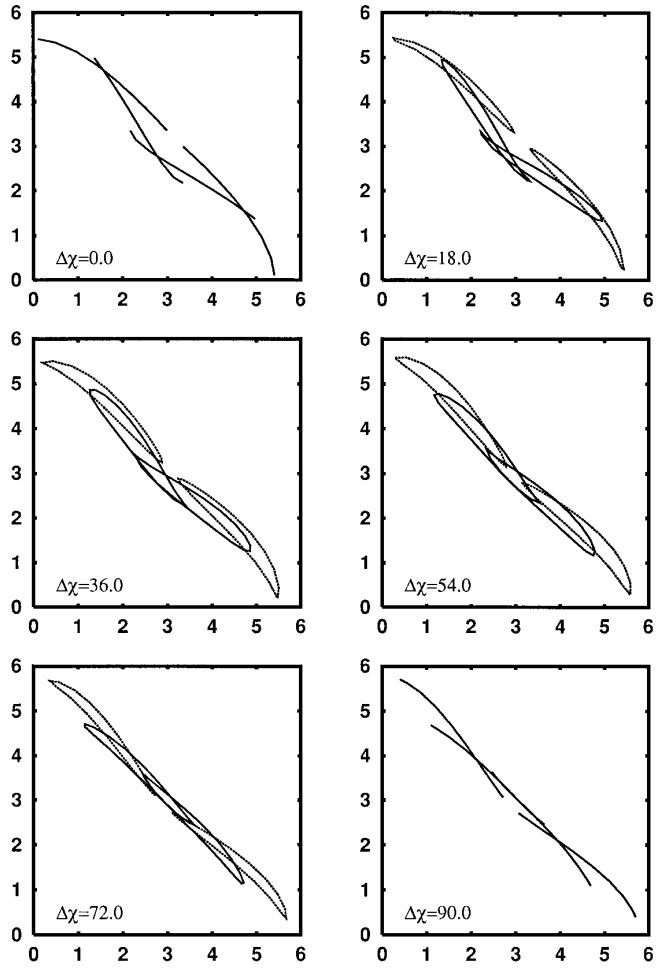

FIG. 5. Schematic representation of the ss+ 2D correlation features in the ⊥ HYSCORE spectrum as dependent on the $\Delta\chi$ angle between the axis of maximum HFI and maximum NQI in the ⊥ plane. The lines in the 2D frequency domain connect the (ν_α, ν_β) coordinates calculated in first order (Eq. [13]) while varying the angle (χ) of the B field through the xy plane. First-order parameters: $A_\perp(\text{av}) = 5.9$ MHz, $Q_\perp(\text{av}) = 0.3$ MHz, $R = 0.3$ MHz, and $J = 0.8$ MHz.

$$Q_\perp(1, 2) = -\tfrac{1}{2}Q_\parallel \pm J$$

$$J = \tfrac{1}{2}K\{[3\sin^2\beta + \eta\cos 2\alpha(1 + \cos^2\beta)]^2 + 4\eta^2\sin^2 2\alpha\cos^2\beta\}^{1/2}. \quad [12]$$

Unfortunately, there is no spectral feature in the 1D spectra from which this parameter can be directly determined. The ss+ correlation ridges in the HYSCORE spectra provide, in principle, a handle on the simultaneous estimation of the R and J parameters. In addition, they yield information about the relative orientation of the HFI and NQI tensors in the ⊥ plane. To describe this behavior one needs the expressions for the effective (i.e., first-order) A and Q splittings for an arbitrary orientation χ of the magnetic field B_0 in the ⊥ plane:

$$T_\perp(\chi) = -\frac{T_\parallel}{2} + R\cos 2(\chi + \psi - \psi_0)$$

$$\cos(2\psi_o) = \{3(T_1 + T_2)\sin^2\theta - (T_1 - T_2)\cos 2\phi\,(\cos^2\theta + 1)\}/\{2\sin 2\phi\cos\theta(T_1 - T_2)\}$$

$$Q_\perp(\chi) = -\frac{Q_\parallel}{2} + J\cos 2(\chi + \gamma - \gamma_0) \quad [13]$$

$$\cot(2\gamma_0) = -\frac{3\sin^2\beta + \eta\cos 2\alpha(\cos^2\beta + 1)}{2\eta\sin 2\alpha\cos\beta}.$$

Since the EPR spectrum has virtual axial anisotropy, only the relative orientation $\Delta\chi = |\gamma - \gamma_0 - \psi + \psi_0|$ of the A and Q tensor in the ⊥ plane is relevant. In Fig. 5 a schematic presentation is given for the relationship between $\Delta\chi$ and the ss+ correlation features. The correlations are patterns formed by a set of coordinates $(\nu^{(1)}_{sq+}, \nu^{(2)}_{sq-})$ and $(\nu^{(2)}_{sq+}, \nu^{(1)}_{sq-})$ calculated using only the first-order contributions in Eqs. [4] and [13]. For angles $\Delta\chi = 0°$ or 90° the patterns are simplified to narrow ridges. In this case, the angles with the positive diagonal represent the ratio between the R and J parameters. For angles other than 0° or 90° the ridges open up to give ellipsoids with varying angles with respect to the diagonal. In the experimental HYSCORE spectrum, the rather broad ss+ correlation ridge shows a distinct splitting, suggesting a $\Delta\chi$ value below 18° or above 72°. Although the ss+ feature is much less affected by dead time artifacts than the single-quantum lines in the 1D ESEEM experiments, the lineshapes in the 2D frequency domain are not well defined and an accurate estimation of the $\Delta\chi$ value is not possible. For the same reason the J parameter extracted from the projections of the ss+ feature would suffer from a large experimental error. Therefore, it was decided not to attempt an estimation for J since, moreover, it is not required for our fitting strategy (see below). For $\Delta\chi$ a starting value of 20° was taken, as indicated in Table 2.

TABLE 2
Summary of Constraint Parameters and Starting Values

Parameter	First- or Second-order estimation	Recalculated from fit values (Table 3)
$A_\parallel$	−6.45 ± 0.03 MHz	−6.55 MHz
$A^{(2)}$	1.00 ± 0.10 MHz^2	0.87 MHz^2
$Q_\parallel$	0.46 ± 0.03 MHz	−0.56 MHz
Q_q	1.15 ± 0.10 MHz^2	1.01 MHz^2
$A_\perp$(av)	6.03 ± 0.05 MHz	6.00 MHz
R	0.40 ± 0.10 MHz	0.30 MHz
a	6.17 ± 0.10 MHz	6.18 MHz
$T_\parallel$	0.28 ± 0.05 MHz	0.37 MHz
J		0.82 MHz
$\Delta\chi$	20 ± 20°	27°

Determination of tensor principal values. From a bookkeeping argument we learn that, given the six constraint parameters ($Q_\parallel$, Q_q, $A_\parallel$, a, R, and $\Delta\chi$), the number of free fitting parameters will be reduced to 4. The next step on the way to the final fit of the experimental ESEEM spectra is now to translate the ''constraint parameters'' into principal values of hyperfine and quadrupole tensors as a function of the Euler angles. From $Q_\parallel$ and Q_q, a set of principal parameters K, η can be calculated for any combination of Euler angles (α, β) using Eq. [10]:

$$\eta^2\left(\frac{Q_\parallel^2}{Q_q} - B^2\right) - \eta(2BC) + 3\,\frac{Q_\parallel^2}{Q_q} - C^2 = 0$$

$$B = -\cos 2\alpha \sin^2\beta; \quad C = 3\sin^2\beta - 2$$

$$Q_q = K^2(3 + \eta^2) \rightarrow K = \left\{\frac{Q_q}{3 + \eta^2}\right\}^{1/2}. \qquad [14]$$

Since we are dealing with a quadratic equation in η, there will be up to two solutions for each combination of (α, β). Imposing a given order of the principal values (e.g., $|Q_1| < |Q_2| < |Q_3|$) a unique solution can be selected. Thus, for each $Q_\parallel$ and Q_q, and a given principal order, a table of K and η can be generated over a grid of (α, β) combinations. The third angle γ characterizing the orientation of the quadrupole tensor is irrelevant in an axial EPR system, and will be set to zero. For future use, the table will be extended with the calculated values of γ_0 using Eq. [13]. The quadrupole interaction is now completely defined in this ''Q table.''

For the analogous generation of an ''A table'' we turn to Eqs. [9] and [11]. Given the $T_\parallel$ and R a series of T_1, T_2 values can be calculated over a grid of (ϕ,θ) values. In this case the two equations were solved for every (ϕ, θ) using computer code produced by the symbolic algebra program MAPLE (see Appendix). In the same procedure, the remaining parameter ψ is calculated from ψ_0 (Eq. [13]), γ_0 (Q table), and the estimated value of $\Delta\chi$ (20°):

$$\psi = \psi_0 - \gamma_0 \pm \Delta\chi. \qquad [15]$$

The A table is thus linked to the Q table only through parameter γ_0. In the Appendix examples of the Q and A tables are listed.

In summary, one can formulate this procedure as a kind of parameter mapping:

$$Q[Q_q, Q_\parallel](\alpha, \beta) \rightarrow (K, \eta, \gamma_0)$$
$$A[A_\parallel, R, a](\phi, \theta) \rightarrow (T_1, T_2, \psi_0)$$
$$A[\gamma_0, \psi_0, \Delta\chi] \rightarrow \psi. \qquad [16]$$

It is now feasible to perform a grid search over (α, β, ϕ, θ) using a coarse grid of say 10–20 values for each angle. Subsequently, one can perform a nonlinear least-squares optimization (e.g., a simplex fit) starting from the best grid value relaxing all parameters (including positional constraints). This procedure can be repeated several times. When we consider the accuracy of the determined constraint parameters we must realize that the values extracted from the $\parallel$ positions (Q_q, $Q_\parallel$, and $A_\parallel$) are better determined than those at the $\perp$ positions ($A_\perp$(av) and especially R). The A table which strongly depends on the latter parameters is therefore less reliable as a search grid than the Q table. To reduce the number of cycles optimizing the A parameters we can, in this particular case, impose another constraint to the fit variables. Since the local symmetry around the ^{14}N nuclei is determined by the quinoline ligand plane, it is assumed that the **A** and **Q** tensors share a principal axis orientation (z by definition) $\perp$ to the ligand plane. This means that $\beta = \theta$ and $\gamma = \psi$ (=0). The search is now driven only by one table, preferably the Q table. For every (α, β, K, η) combination, the ϕ value from the A table is selected which is connected to a ψ_0 value satisfying the relation $\|\psi_0 - \gamma_0\| = \Delta\chi$. The parameter mapping procedure is now summarized as

$$Q[Q_q, Q_\parallel](\alpha, \beta) \rightarrow (K, \eta, \gamma_0)$$
$$A[A_\parallel, R, a, \theta = \beta](\phi) \rightarrow (T_1, T_2, \psi_0). \qquad [17]$$

The constraint parameters derived from the experimental spectra using the second-order analyses as described above are presented in Table 2. Obviously, there are nine possibilities of aligning two tensors along one axis. These were all investigated, leading to the following order of the principal values: $|Q_x| > |Q_z| > |Q_y|$ and $|A_z| > |Q_x| > |Q_y|$ in combination with coinciding A_z and Q_z axes. In the Appendix, the A and Q tables corresponding to these constraints are listed. The grid search on the Q table assuming coinciding Q_z and A_z axes led to the following best-fit angles: (α, β, ϕ, θ, ψ) = (50°, 30°, 25°, 30°, 0). Inspection of the A and Q table (see Appendix) leads to a $\Delta\chi$ value of 22°. The complete parameter set was used as a starting point for a simplex optimization. In Table 3, the interaction parameters for which conversion was obtained are listed. Relaxing the constraint of coinciding z axes of the A and Q tensor, i.e., releasing the θ, γ, and ψ, did not lead to an improvement of the fit. Therefore, one may conclude that the additional constraint of coinciding axes produced a reliable ''minimal number of parameters'' fit.

DISCUSSION

The grid search on both A and Q tables can now be used to probe the ''maximum likelihood'' parameter space of the fit values. In Fig. 6 the relevant 2D slices through the best-fit point (α, β, ϕ, θ) in the 4D parameter space are presented. It

TABLE 3
^{14}N Best-Fit Parameters (MHz)

Tensor	1	2	3	iso	(Euler angles in °)		
					ϕ	θ	ϕ
HFI	−6.12	−5.67	−6.75	−6.18	21	33	0
					α	β	γ
NQI	−1.17	+0.51	+0.66		72	33	0
		$K = 0.58$ MHz, $\eta = 0.13$					
				VO polar angle (X ray):	63	22	

is striking that an extended range of (α, β) values comes rather close to the best-fit RMS value. This can be explained by the near axiality of the obtained **Q** tensor ($\eta = 0.13$). This means that best-fit *angles* for the quadrupole tensor are not necessarily unique. In Table 2, the constraint parameters as derived from the second-order analysis of the peak positions in the ESEEM spectra are compared to the recalculated values based on the best-fit values. Since the simulated peak positions match the experimental ones extremely well, one must conclude that the deviations in the constraint parameters are mainly due to the limitations of the second-order perturbation theory under the interactions of our spin system. Most deviations are, however, within the experimental error margins (estimated from the variations in the parameters over the different multifrequency spectra). It is interesting to note that the $\|$ C-band spectra provided the most accurate estimations of the $Q_\|$ splitting. This is because the single-quantum transitions were most prominent in these spectra (as compared to the X-band ones) and were not subject to overlap with other resonances.

The Euler angles α and β of the quadrupole tensor can be related to the geometrical structure of the complex if one can assume that the principal directions are fixed on the ligand plane: i.e., the *X* axis bisecting the C12−N2−C11 pattern as shown in Fig. 1; the *Y* axis perpendicular to that in the ligand plane and the *Z* axis perpendicular to the ligand plane. In this picture, one can regard the Euler angles α and β as the polar angles of the V = O bond (i.e., the *z* axis in the laboratory frame) in the principal axis frame of the *Q* tensor. The coordination angles as determined from the X-ray structure are presented in Table 3 together with the experimental Euler angles. Note that the X-ray data are well within the parameter space as defined by the error profile in Fig. 6a.

Reviewing the obtained hyperfine and quadrupole tensors allows the following conclusions: The isotropic hyperfine coupling $a = 6$ MHz matches the typical values (6−7 MHz) found for equatorially coordinated pyridine and imidazole rings (aza aromatic ligands). The principle components (0.06; 0.51; −0.57) MHz of the anisotropic part are much smaller than the isotropic part. The hyperfine tensor is characterized by a significant deviation from axiality. This result correlates with data obtained from other nitrogen-coordinated oxovanadium complexes: VO^{2+}-porphyrines ($a = 7.2$ MHz and (0, 0.5, −0.5) MHz) (*7*) and VO^{2+}-histidine in D-xylose isomerase ($a = 5.65$ MHz and (0.0, 0.4, −0.4)

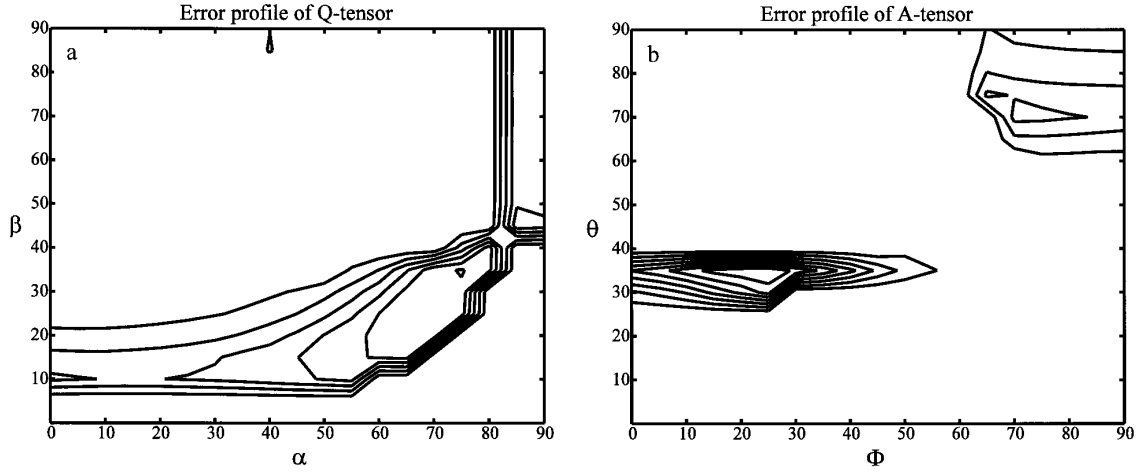

FIG. 6. (a) Fitting profiles over the α and β Euler angles of the NQI fixing the HFI at the best-fit value (Table 3). (b) Fitting profiles over the ϕ and θ Euler angles of the HFI fixing the NQI at the best-fit value (Table 3). The contour lines represent the inverse RMS value.

MHz) (*16*). This kind of hyperfine tensor results from indirect spin transfer from the VO^{2+}-d_{xy} orbital to the nitrogen 2*s* and 2*p* orbitals in combination with the ''through space'' dipolar coupling between the unpaired electron and the nitrogen nucleus (*7*).

The obtained nitrogen quadrupole coupling constant $K = 0.58$ MHz follows the same tendency as other pyridine-like complexes with VO^{2+} (assuming that quinoline has a K value similar to that of pyridine). It was found that the K value for metal-coordinated pyridine is always lower than that of the uncoordinated base ($K = 0.65-0.8$ MHz in Zn^{2+} and Cd^{2+} complexes versus 1.15 MHz for free pyridine) (*1, 34*). For imidazole a similar trend is observed (*34*). The axis of the largest principal value (x) is directed toward the metal along the vanadium–nitrogen bond. The middle principal value (z) is oriented along the normal to the ligand plane. This is in contrast to the hyperfine tensor of which the maximum principal value is oriented along the normal to the ligand plane. In the ligand plane the two tensors are 50° off with respect to each other. It seems that the hyperfine components in the *xy* plane follow more or less the nitrogen carbon bonds of the quinoline ligand.

CONCLUSIONS

We have demonstrated that using orientation-selective multifrequency 1D and 2D ESEEM combined with perturbation analysis, it is possible to devise a systematic strategy using a 4D grid search for finding the best simulation parameters for the ESEEM of $VO(meox)_2$. The resulting angular profiles (Figs. 6a and 6b) give a good indication of the total parameter space consistent with the experimental spectra. The limitations of the second-order analysis lead to a spread in the estimated constraint parameters over the multifrequency ESEEM spectra. In most cases, the error margins estimated from these variations enclose the best-fit parameters resulting from a simplex optimization starting from the optimum grid search values.

The correspondence between the NQI Euler angles and the geometry of the complex based on the X-ray structure indicates that for $VO(meox)_2$, the NQI tensor of the coordinating nitrogen of the quinoline ligand follows the local symmetry and is fixed on the ligand plane.

Obviously, the second-order approach will not be valid for all ^{14}N spin systems, but it is to be expected that strategies based on positional constraints can be developed for a wider range of NQI and HFI interactions. The simulation strategy discussed in this article is applicable with minor modifications to the analysis of orientationally selected X-band ESEEM spectra of any number of nitrogens with hyperfine couplings $\geq 4-5$ MHz. The data obtained from such analysis will form a reliable basis for the establishment of a detailed geometry of nitrogen ligation. Therefore, one can envisage further development of this approach in the study of active sites in metalloproteins and inorganic model complexes. We anticipate future applications of this method to VO^{2+} as spin probe in proteins as well as other metal centers including hemes, the mixed-valent diiron centers, and iron–sulfur centers.

APPENDIX

Generating *Q* and *A* Tables

The parameter mappings of Eq. [16] lead to the *Q* and *A* tables: The program for generating the *Q* tables takes as input the constraint parameters Q_q and $Q_\parallel$ and produces for every combination of α and β the set of corresponding K and η values by solving Eq. [14]. The final output for the ESEEM simulation program is given below:

Q-TABLE Qq=1.1 MHZ, Q//=0.46 MHZ

ALPHA	BETA	PX	PY	PZ	GAMMAO
0.	20.0000	1.20779	-.526849	-.680939	0.
5.00000	20.0000	1.20794	-.528728	-.679212	84.6196
10.0000	20.0000	1.20837	-.534315	-.674055	79.2614
15.0000	20.0000	1.20901	-.543458	-.665549	73.9454
20.0000	20.0000	1.20974	-.555903	-.653836	68.6868
25.0000	20.0000	1.21043	-.571295	-.639132	63.4951
30.0000	20.0000	1.21091	-.589177	-.621737	58.3740
0.	25.0000	1.18265	-.365464	-.817181	0.
5.00000	25.0000	1.18334	-.368574	-.814770	84.1218
10.0000	25.0000	1.18538	-.377854	-.807527	78.3156
15.0000	25.0000	1.18858	-.393147	-.795433	72.6402
20.0000	25.0000	1.19265	-.414167	-.778487	67.1333
25.0000	25.0000	1.19721	-.440467	-.756747	61.8090
30.0000	25.0000	1.20179	-.471405	-.730389	56.6615
35.0000	25.0000	1.20589	-.506125	-.699764	51.6707
40.0000	25.0000	1.20901	-.543552	-.665461	46.8083
45.0000	25.0000	1.21077	-.582433	-.628337	42.0432
0.	30.0000	1.10503	-.123354	-.981677	0.
5.00000	30.0000	1.10679	-.127655	-.979139	82.5384
10.0000	30.0000	1.11202	-.140602	-.971415	75.4329
15.0000	30.0000	1.12050	-.162313	-.958190	68.9036
20.0000	30.0000	1.13187	-.192903	-.938967	63.0018
25.0000	30.0000	1.14551	-.232370	-.913136	57.6616
30.0000	30.0000	1.16052	-.280422	-.880094	52.7665

Q-TABLE Qq=1.1 MHZ, Q//=0.46 MHZ

ALPHA	BETA	PX	PY	PZ	GAMMAO
35.0000	30.0000	1.17570	-.336279	-.839426	48.1928
40.0000	30.0000	1.18965	-.398497	-.791156	43.8294
45.0000	30.0000	1.20090	-.464903	-.736000	39.5846
50.0000	30.0000	1.20825	-.532713	-.675537	35.3865
55.0000	30.0000	1.21104	-.598838	-.612197	31.1815
35.0000	35.0000	1.06616	-.356188E-01	-1.03055	38.5669
40.0000	35.0000	1.10762	-.129675	-.977942	36.5544
45.0000	35.0000	1.14793	-.239765	-.908166	34.2414
50.0000	35.0000	1.18145	-.360225	-.821226	31.5870
55.0000	35.0000	1.20319	-.482231	-.720960	28.5794
60.0000	35.0000	1.21101	-.596321	-.614693	25.2307
55.0000	40.0000	1.10524	-.123865	-.981376	21.6065
60.0000	40.0000	1.19454	-.424622	-.769918	21.9082
0.	50.0000	1.21106	-.604347	-.606712	0.
70.0000	50.0000	1.19848	-.448445	-.750033	11.8398
75.0000	50.0000	1.14617	-.234379	-.911791	7.53707
80.0000	50.0000	1.10984	-.135167	-.974673	4.61433
85.0000	50.0000	1.08953	-.868314E-01	-1.00269	2.20678
90.0000	50.0000	1.08301	-.721308E-01	-1.01088	0.
0.	55.0000	1.13925	-.213846	-.925406	0.
5.00000	55.0000	1.14458	-.229591	-.914994	40.4966
10.0000	55.0000	1.16050	-.280370	-.880131	46.4021
15.0000	55.0000	1.18571	-.379383	-.806326	50.6128
20.0000	55.0000	1.21010	-.563305	-.646796	55.5278
70.0000	55.0000	1.21099	-.594438	-.616555	11.6906
75.0000	55.0000	1.19169	-.409029	-.782664	7.51817
80.0000	55.0000	1.16843	-.308400	-.860032	4.60244
85.0000	55.0000	1.15330	-.256603	-.896694	2.19980
90.0000	55.0000	1.14818	-.240517	-.907658	0.
20.0000	60.0000	1.08534	-.773447E-01	-1.00800	16.4566
25.0000	60.0000	1.16398	-.292394	-.871584	27.3334
75.0000	60.0000	1.20390	-.488060	-.715839	6.90381
80.0000	60.0000	1.18937	-.397071	-.792298	4.23215
85.0000	60.0000	1.17860	-.348096	-.830502	2.02298
90.0000	60.0000	1.17478	-.332609	-.842174	0.
30.0000	65.0000	1.05196	-.633521E-02	-1.04563	10.8183
75.0000	65.0000	1.20793	-.528646	-.679287	6.01075
80.0000	65.0000	1.19811	-.446078	-.752030	3.68566
85.0000	65.0000	1.19003	-.400407	-.789623	1.76143
90.0000	65.0000	1.18707	-.385793	-.801273	0.
75.0000	70.0000	1.20951	-.551792	-.657723	4.95773
80.0000	70.0000	1.20230	-.475199	-.727097	3.03808
85.0000	70.0000	1.19583	-.432134	-.763701	1.45128
90.0000	70.0000	1.19340	-.418251	-.775151	0.
40.0000	75.0000	1.17292	-.325329	-.847593	10.0158
75.0000	75.0000	1.21021	-.565719	-.644487	3.79989
80.0000	75.0000	1.20449	-.493144	-.711346	2.32625
85.0000	75.0000	1.19901	-.451929	-.747082	1.11063
90.0000	75.0000	1.19691	-.438581	-.758326	0.
40.0000	80.0000	1.20663	-.513657	-.692970	9.50136
45.0000	80.0000	1.08251	-.710061E-01	-1.01150	3.87582
75.0000	80.0000	1.21052	-.574058	-.636466	2.57086
80.0000	80.0000	1.20568	-.504042	-.701634	1.57233
85.0000	80.0000	1.20078	-.464042	-.736740	0.750317
90.0000	80.0000	1.19888	-.451051	-.747827	0.
40.0000	85.0000	1.21086	-.586337	-.624523	5.64668
45.0000	85.0000	1.13046	-.189006	-.941454	2.34550
75.0000	85.0000	1.21066	-.578536	-.632129	1.29653
80.0000	85.0000	1.20627	-.509941	-.696329	0.792418
85.0000	85.0000	1.20169	-.470628	-.731061	0.378016
90.0000	85.0000	1.19989	-.457841	-.742051	0.
45.0000	90.0000	1.14206	-.222056	-.920000	0.
75.0000	90.0000	1.21070	-.579951	-.630754	0.
80.0000	90.0000	1.20645	-.511312	-.694639	0.
85.0000	90.0000	1.20197	-.472721	-.729249	0.
90.0000	90.0000	1.20021	-.460000	-.740206	0.

The program for generating the A tables takes as input the constraint parameters $A_{\|}$, R, and a and produces for every combination of ϕ and θ the set of corresponding T_1, T_2, and T_3 values by solving the equation

$$R^2(TT)^2 - \tfrac{1}{4}T_{\|}^2(RR)^2 = 0, \qquad [18]$$

where

$$TT = \{[3(1+s) + (1-s)\cos 2\phi]\sin^2\theta - 2(1+s)\}^{1/2}$$

$$RR = \{[-3(1+s)\sin^2\theta + (1-s)\cos 2\phi(1+\cos^2\theta)]^2 + 4(1-s)^2\sin^2 2\phi\cos^2\theta\}^{1/2}$$

$$s = T_2/T_1 \quad \text{with } 0 < s < 1. \qquad [19]$$

Equation [18] is solved for s using computer code generated by MAPLE. This code is available from the authors (E.J.R.) upon request. Below the A table for the ESEEM simulation program is listed:

A-TABLE: A-ISO=6.0 MHZ, T//=0.5 MHZ, R=0.35 MHZ

PHI	THETA	AX	AY	AZ	PSI0
0.	25.0000	-5.98886	-5.40000	-6.61114	0.
5.00000	25.0000	-5.98938	-5.39861	-6.61201	-3.81629
10.0000	25.0000	-5.99096	-5.39444	-6.61460	-7.65819
15.0000	25.0000	-5.99359	-5.38747	-6.61894	-11.5514
20.0000	25.0000	-5.99728	-5.37764	-6.62507	-15.5216
0.	30.0000	-5.90000	-5.40000	-6.70000	0.
5.00000	30.0000	-5.90075	-5.39823	-6.70102	-3.09882
10.0000	30.0000	-5.90301	-5.39287	-6.70413	-6.23297
15.0000	30.0000	-5.90680	-5.38379	-6.70941	-9.43825
20.0000	30.0000	-5.91218	-5.37077	-6.71705	-12.7513
25.0000	30.0000	-5.91921	-5.35352	-6.72728	-16.2102
30.0000	30.0000	-5.92796	-5.33167	-6.74037	-19.8541
35.0000	30.0000	-5.93850	-5.30484	-6.75666	-23.7242
40.0000	30.0000	-5.95089	-5.27266	-6.77645	-27.8624
45.0000	30.0000	-5.96515	-5.23485	-6.80000	-32.3115
50.0000	30.0000	-5.98121	-5.19136	-6.82743	-37.1137
55.0000	30.0000	-5.99890	-5.14253	-6.85858	-42.3079
0.	35.0000	-5.71524	-5.40000	-6.88476	0.
5.00000	35.0000	-5.71622	-5.39832	-6.88546	-1.85194
10.0000	35.0000	-5.71920	-5.39316	-6.88764	-3.74903
15.0000	35.0000	-5.72429	-5.38422	-6.89149	-5.73861
20.0000	35.0000	-5.73167	-5.37093	-6.89739	-7.87232
25.0000	35.0000	-5.74161	-5.35248	-6.90591	-10.2077
30.0000	35.0000	-5.75440	-5.32775	-6.91786	-12.8094
35.0000	35.0000	-5.77038	-5.29526	-6.93436	-15.7487
40.0000	35.0000	-5.78990	-5.25323	-6.95687	-19.1024
45.0000	35.0000	-5.81327	-5.19960	-6.98714	-22.9501
50.0000	35.0000	-5.84074	-5.13216	-7.02710	-27.3724
55.0000	35.0000	-5.87245	-5.04895	-7.07861	-32.4494
60.0000	35.0000	-5.90830	-4.94875	-7.14295	-38.2602
65.0000	35.0000	-5.94776	-4.83224	-7.22000	-44.8788
70.0000	35.0000	-5.98938	-4.70362	-7.30701	-52.3632
70.0000	40.0000	-5.67717	-4.53068	-7.79215	-26.8767
75.0000	40.0000	-5.82143	-4.01242	-8.16616	-40.9138
80.0000	40.0000	-5.95192	-3.46177	-8.58631	-55.6228
85.0000	40.0000	-5.40238	-5.14487	-7.45275	-1.40241
90.0000	40.0000	-5.40000	-5.14825	-7.45175	-.966576E-15
90.0000	45.0000	-5.00000	0.286463E+08	-.286463E+08	-.473768E-07
85.0000	50.0000	-6.03442	-9.03839	-2.92719	75.6899
90.0000	50.0000	-6.10000	-9.11732	-2.78268	90.0000
80.0000	55.0000	-6.01828	-7.57136	-4.41036	77.0994
85.0000	55.0000	-6.08089	-7.56178	-4.35732	83.9180
90.0000	55.0000	-6.10000	-7.55809	-4.34191	90.0000
80.0000	60.0000	-6.05837	-7.07518	-4.86646	82.8084
85.0000	60.0000	-6.09014	-7.05608	-4.85378	86.5595
90.0000	60.0000	-6.10000	-7.05000	-4.85000	90.0000
75.0000	65.0000	-6.03380	-6.85779	-5.10841	82.7986
80.0000	65.0000	-6.07299	-6.82720	-5.09981	85.5202
85.0000	65.0000	-6.09356	-6.81082	-5.09562	87.8437
90.0000	65.0000	-6.10000	-6.80565	-5.09435	90.0000
70.0000	70.0000	-6.00207	-6.75447	-5.24345	83.1658
75.0000	70.0000	-6.05118	-6.71151	-5.23731	85.3583
80.0000	70.0000	-6.07993	-6.68597	-5.23410	87.0936
85.0000	70.0000	-6.09520	-6.67229	-5.23251	88.5967
90.0000	70.0000	-6.10000	-6.66797	-5.23203	90.0000
70.0000	75.0000	-6.02131	-6.65942	-5.31928	85.6385
75.0000	75.0000	-6.06045	-6.62260	-5.31696	87.0174
80.0000	75.0000	-6.08366	-6.60062	-5.31572	88.1259
85.0000	75.0000	-6.09608	-6.58881	-5.31510	89.0935
90.0000	75.0000	-6.10000	-6.58509	-5.31491	90.0000
70.0000	80.0000	-6.03187	-6.60194	-5.36620	87.3923
75.0000	80.0000	-6.06560	-6.56900	-5.36541	88.2101
80.0000	80.0000	-6.08575	-6.54927	-5.36498	88.8731
85.0000	80.0000	-6.09658	-6.53865	-5.36477	89.4544
90.0000	80.0000	-6.10000	-6.53530	-5.36470	90.0000
70.0000	85.0000	-6.03726	-6.57091	-5.39184	88.7761
75.0000	85.0000	-6.06824	-6.54009	-5.39167	89.1584
80.0000	85.0000	-6.08683	-6.52159	-5.39158	89 4696
85.0000	85.0000	-6.09684	-6.51164	-5.39153	89.7431
90.0000	85.0000	-6.10000	-6.50848	-5.39152	90.0000
70.0000	90.0000	-6.03892	-6.56108	-5.40000	90.0000
75.0000	90.0000	-6.06906	-6.53094	-5.40000	90.0000
80.0000	90.0000	-6.08716	-6.51284	-5.40000	90.0000
85.0000	90.0000	-6.09691	-6.50309	-5.40000	90.0000
90.0000	90.0000	-6.10000	-6.50000	-5.40000	90.0000

ACKNOWLEDGMENTS

This research was financially supported by the Netherlands Organization for Chemical Research (SON). A.M.T. thanks the Netherlands Organization for Scientific Research NWO for supporting his stay in Nijmegen (Grant 07-13-089) during 1993–1994. Part of this work was sponsored by the U.S. Department of Energy under Contract DE-AC06-76 RLO 1830 and by Associated Western Universities Inc., North-West Division (AWU-NW), under Grant DE-FG06-89ER-75522 or DE-FG06-92RL-12451 with the U.S. Department of Energy. S.A.D. acknowledges the receipt of a Faculty Fellowship from the AWU-NW.

REFERENCES

1. A. V. Astashkin, S. A. Dikanov, and Yu. D. Tsvetkov, *J. Struct. Chem.* **26,** 363–368 (1985).
2. E. J. Reijerse, J. J. Shane, E. de Boer, and D. Collison, *in* ''Electron Magnetic Resonance of Disordered Systems'' (N. D. Yordanov, Ed.), p. 189, World Scientific, Singapore (1989).
3. E. J. Reijerse, J. J. Shane, E. de Boer, P. Höfer, and D. Collison, *in* ''Electron Magnetic Resonance of Disordered Systems'' (N. D. Yordanov, Ed.), pp. 253–271, World Scientific, Singapore (1991).
4. S. A. Cosgrove-Larsen and D. J. Singel, *J. Phys. Chem.* **96,** 9007 (1992).
5. A. Togni, G. Rist, G. Rihs, and A. Schweiger, *J. Am. Chem. Soc.* **115,** 1908 (1993).
6. S. A. Dikanov, C. Burgard, and J. Hüttermann, *Chem. Phys. Lett.* **212,** 493 (1993).
7. K. Fukui, H. Ohya-Nishiguchi, and H. Kamada, *J. Phys. Chem.* **97,** 1185 (1993).
8. V. Kofman, S. A. Dikanov, A. Haran, J. Libman, A. Shanzer, and D. Goldfarb, *J. Am. Chem. Soc.* **117,** 383 (1994).
9. S. A. Dikanov, R. I. Samoilova, J. A. Smeija, and M. K. Bowman, *J. Am. Chem. Soc.* **117,** 10579 (1995).
10. S. S. Eaton, J. Dubach, K. More, G. R. Eaton, G. Thurman, and D. R. Ambroso, *J. Biol. Chem.* **264,** 4776 (1989).
11. E. de Boer, C. P. Keijzers, A. A. K. Klaassen, E. J. Reijerse, D. Collison, C. D. Garner, and R. Wever, *FEBS Lett.* **235,** 93 (1988).
12. P. A. Tipton, J. McCracken, J. B. Cornelius, and J. Peisach, *Biochemistry* **28,** 5720 (1989).
13. G. I. Gerfen, P. M. Hanna, N. D. Chasteen, and D. J. Singel, *J. Am. Chem. Soc.* **113,** 9513 (1991).
14. C. Zhang, G. D. Markham, and R. LoBrutto, *Biochemistry* **32,** 9886 (1993).
15. A. L. P. Houseman, L. Morgan, R. LoBrutto, and W. D. Frash, *Biochemistry* **33,** 4910 (1994).
16. S. A. Dikanov, A. M. Tyryshkin, J. Hüttermann, R. Bogumil, and H. Witzel, *J. Am. Chem. Soc.* **117,** 4976 (1995).
17. K. Fukui, H. Ohya-Nishiguchi, M. Nakai, H. Sakurai, and H. Kamada, *FEBS Lett.* **368,** 31 (1995).
18. C. Buy, T. Matsui, S. Adrianambinintsoa, C. Sigalat, G. Girault, and J.-L. Zimmermann, *Biochemistry* **35,** 14281 (1996).
19. C. A. McDowell, A. Naito, D. L. Sastry, and K. Takegoshi, *J. Magn. Reson.* **117,** 283 (1986).
20. C. A. McDowell, A. Naito, D. L. Sastry, Y. U. Cui, and S. X. Yu K. Sha, *J. Mol. Struct.* **195,** 361 (1989).
21. M. J. Colaneri and J. Peisach, *J. Am. Chem. Soc.* **114,** 5335 (1992).
22. J. J. Shane, P. A. A. W. Vanderheijden, E. J. Reijerse, and E. de Boer, *Appl. Magn. Reson.* **6,** 427 (1994).
23. M. Shiroo and Q. Fernando, *Anal. Chem.* **43,** 1222 (1971).
24. J. J. Shane, ''Electron Spin Echo Envelope Modulation Spectroscopy of Disordered Solids,'' Ph.D. thesis, University of Nijmegen, The Netherlands (1994).
25. W. B. Mims, *Phys. Rev. B* **5,** 2409 (1972).
26. W. B. Mims, *Phys. Rev. B* **6,** 3543 (1972).
27. J. J. Shane, P. Höfer, E. J. Reijerse, and E. de Boer, *J. Magn. Reson.* **99,** 596 (1992).
28. W. R. Hagen, Personal communication.
29. D. Collison, B. Gahan, and F. E. Mabbs, *J. Chem. Soc. Dalton Trans.,* 111 (1987).
30. S. Dikanov, L. Xun, A. Karpiel, A. Tyryshkin, and M. Bowman, *J. Am. Chem. Soc.* **118,** 8408 (1996).
31. P. Höfer, *J. Magn. Reson. A* **111,** 77 (1994).
32. E. J. Reijerse and S. A. Dikanov, *Pure Appl. Chem.* **64,** 789 (1992).
33. A. Messiah, ''Mecanique quantique,'' Dunod, Paris (1959–1960).
34. E. A. C. Lucken, ''Nuclear Quadrupole Coupling Constants,'' Academic Press, San Diego (1969).